Observations and Magnetic Field Modeling of the Solar Flare/CME Event on 2010 April 8

Vincent Surges[1,2], Yingna Su[2], Adriaan van Ballegooijen[2]

1. INTRODUCTION

The Sun consists nearly entirely of plasma, a highly conductive, ionized gas consisting of ions and electrons. Plasma is known as the fourth state of matter, and as such, has many interesting features that are introduced in this paper. The lowest layer of the solar atmosphere is the photosphere. This layer is the "surface" of the sun, and is the familiar part of the Sun that we are able to see. When we observe sunspots in visible light, we are observing them from the photosphere. Just above the photosphere of the sun lies the chromosphere. Although this layer of the sun has a reddish color, the chromosphere is only visible to the naked eye during a total solar eclipse. The outermost region of the sun, the corona, extends from about 20,000 km above the sun to millions of kilometers into space. However, like the chromosphere, the corona is only visible during a total solar eclipse or with special instruments.

1.1. Solar Eruptions

We refer to three different types of solar eruptions throughout this paper: solar flares, prominence eruptions, and coronal mass ejections (CMEs). Solar eruptions often occur in regions of the sun where the magnetic field is exceptionally strong, known as active regions. In these regions, the magnetic field lines can become clustered together to essentially form a magnetic plug, prohibiting the upward flow of heat. These areas appear darker when viewed against the rest of the sun.

Figure 1 shows typical images of different types of solar eruptions. The most commonly seen flare morphology is the two-ribbon flare, according to Tang (1985). Figure 1a shows two Hα (red visible spectral line created by hydrogen) ribbons produced by a flare. There is one ribbon on each side of the Polarity Inversion Line (PIL), a hypothetical line dividing regions of opposite magnetic polarity. The ribbons separate over time, and are most easily seen as

[1]Math, The College of St. Scholastica, Duluth, MN55811, USA

[2]Harvard-Smithsonian Center for Astrophysics, Cambridge, MA 02138, USA.

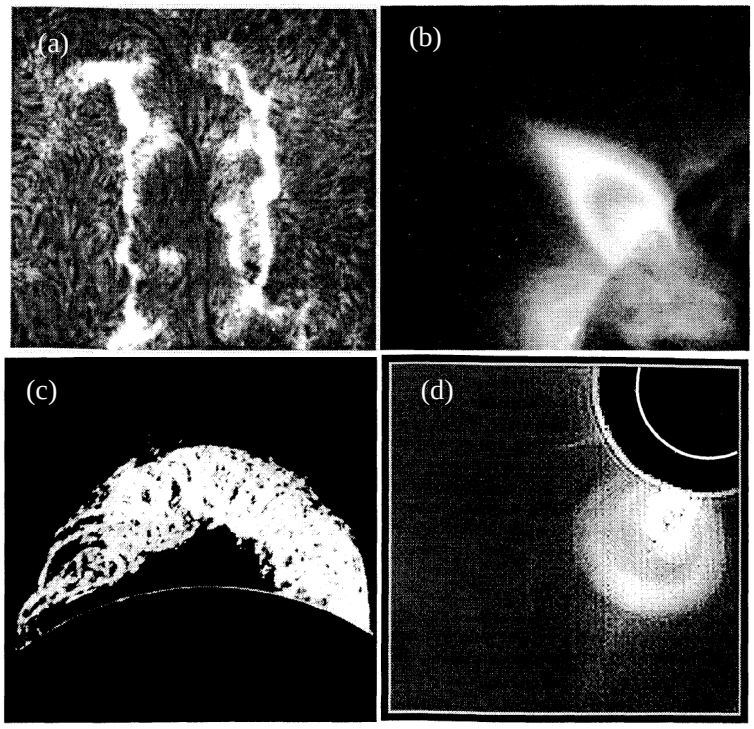

Fig. 1.— Solar eruptive phenomena: (a) Hα ribbons produced by a flare associated with a CME. (b) Cusp-shaped loop system as seen on the limb of the Sun after an eruptive event. Panel (c) shows an Hα image of the large prominence eruption, known as "granddaddy" (June 4, 1946, High-Altitude Observatory). (d) White light coronagraph image of a CME containing an erupted prominence (bright core). The white circular line in the upper right-hand corner indicated the location of the Sun's surface behind the disk of the instrument (Forbes 2000).

being connected by a rising arcade of post-flare loops. Figure 1b shows a cusp-shaped loop system as seen on the limb of the sun after an eruptive event. Another type of solar eruption occurs when prominences erupt (Figure 1c). Solar prominences are large clouds of cool, dense gas anchored in magnetic field lines connecting regions of opposite magnetic polarity. They are well observed in Hα and 304 Å. When seen projected against the solar disk, prominences appear in Hα as dark features called filaments (Su 2007). We use the terms "filament" and "prominence" interchangeably. The most intense explosion occurs during a CME. A CME is a large bubble of gas that is ejected from the Sun's corona into interplanetary space. The bright core in Figure 1d refers to the filament which is ejected during the CME. Often CMEs originate from the same active region of the Sun as solar flares. Although they are generally associated with prominence eruptions and explosive flares, CMEs can occur without being provoked by either of these eruptions (Eddy 2009). CMEs are observed using a white-light coronagraph, an instrument designed to block out the light from the

sun. The coronagraph essentially produces an eclipse of the sun, allowing viewers to observe the corona (see Figure 1d). Extreme Ultraviolet (EUV) observations of the lower corona reveal two dynamic phenomena closely linked to the origins of CMEs: "coronal waves" and "dimmings" (Zhukov & Auchere 2004). In this study, we do not elaborate on coronal waves. Transient dimming of coronal intensity, or "dimmings", have been observed using ground-based coronagraph observations (Attrill 2008). Harvey (1996) stated that "coronal holes expand into areas where the magnetic field was observed previously to be closed" during the formation of large arcades in X-ray observations. Since dimmings generally appear in pairs (Sterling & Hudson, 1997), it is believed that they are footpoints of the expanding flux rope.

1.2. Theory of Solar Eruptions: Magnetic Reconnection

In plasma physics, it is well accepted that magnetic field lines are "frozen in" to plasmas, and are constrained to move as the plasma does. When plasma pushes on two oppositely directed magnetic field lines (see Figure 2), a current sheet is established, allowing plasma diffusion, and thus magnetic reconnection to occur (Priest 1984). Here, the topology of the magnetic field lines change, and high electric current flows in the central diffusion region heating up the plasma. The field lines break apart and reconnect in an entirely new configuration with lower energy. The motion of the plasma is changed dramatically during the course of the event. Originally it pushes the field lines in from the side. After reconnection, it is moving up and down, nearly parallel to the original magnetic field. The middle of the diffusion region, or neutral X region, has zero magnetic polarity, and is thus a null point.

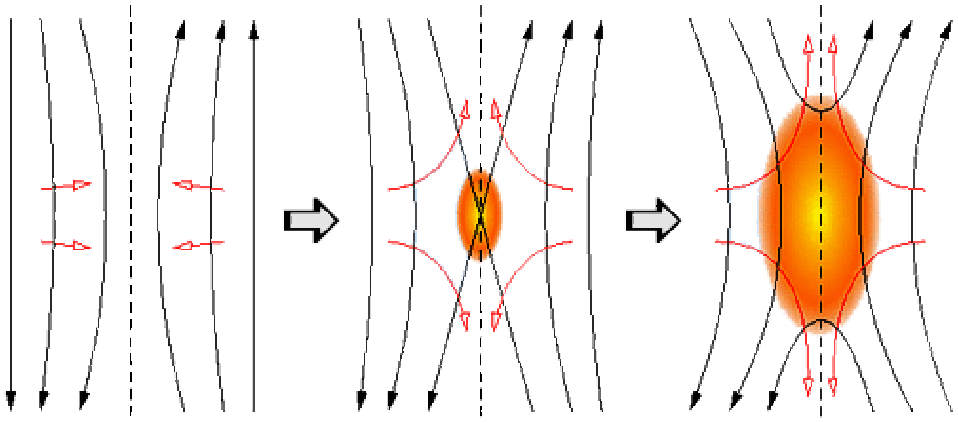

Fig. 2.— Magnetic reconnection shown in three different stages. Initially, plasma from the sides push oppositely directed field lines inwards. Eventually these field lines reconnect into a lower-energy configuration, releasing magnetic free energy in the direction of the original field lines.

Solar eruptions are all thought to be different manifestations of the same physical process involving the disruption of the coronal magnetic field. All involve some form of explosion on the sun, where previously stored energy is converted to kinetic and thermal energy. The coronal magnetic field is constantly stressed due to differential rotation, changing magnetic flux, and connectivity to the interplanetary magnetic field (Sandel et al. 2006). Eventually, the stress will exceed the threshold. When this happens, the magnetic field adjusts by large-scale magnetic reconnection. In the process, free energy that was previously trapped in the solar corona is ejected and converted into kinetic and thermal energy. This heats and accelerates the particles in the plasma, resulting in some form of violent explosion. Figure 3 shows a 2D cartoon of a solar eruption after reconnection has occurred. The part below the reconnection site consists of the post-flare loops and flare ribbons, while the part above the reconnection site represents the CME, which expands into interplanetary space. The inner bright core of the CME refers to the erupting prominence.

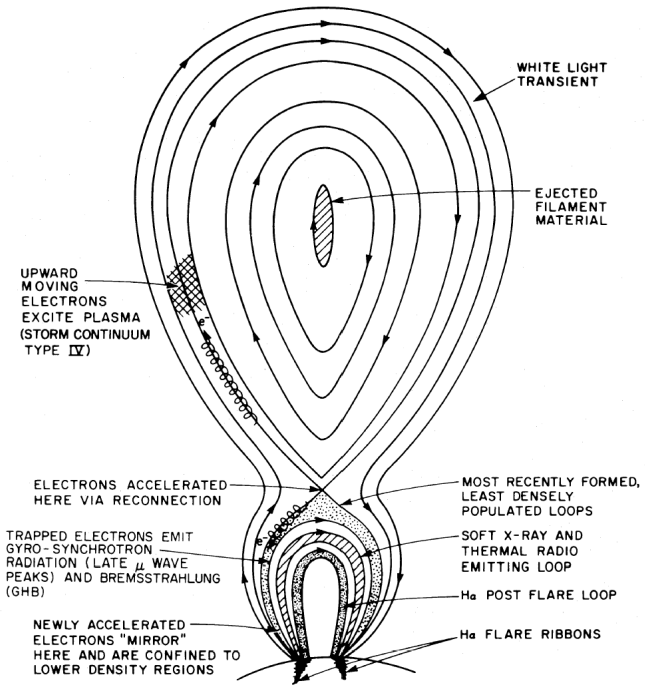

Fig. 3.— 2D cartoon of a typical solar eruption from Cliver et al. (1986). Below the reconnection site, flare ribbons can be seen, acting as footpoints of the post-flare loops. The CME is represented as the large bubble above the reconnection site, containing the ejected filament material in the center.

1.3. MHD—Force Free Equilibrium

We know that the magnetic field lines are frozen in to the plasma, so if we can approximate the motion of the plasma, we can gain a better understanding of the 3D structure of the coronal magnetic field. This can be accomplished by using observations of the motion of the coronal plasma to lead to an indirect calculation of the magnetic field for a particular region of the corona. Treating plasma as a system of individual particles is a tedious and inefficient method to approach this task (Sandell et al. 2006). Instead, the motion of magnetized plasma is calculated by treating the plasma as a fluid. Defining the coronal plasma this way is called magneto-hydrodynamic (MHD) approximation. Using a reduced form of the MHD equations, we can construct force-free fields (i.e., magnetic fields where the Lorentz force $(\mathbf{j} \times \mathbf{B}) = 0$). We begin by listing Gauss's law for magnetism and Ampere's law, two of Maxwell's equations (here in cgs units) that are used in this study

$$\nabla \cdot \mathbf{B} = \mathbf{0}, \tag{1}$$

$$\nabla \times \mathbf{B} = \frac{\mathbf{1}}{\mathbf{c}} \frac{\partial \mathbf{E}}{\partial \mathbf{t}} + \mathbf{4}\pi\mathbf{j}. \tag{2}$$

On the Sun, Maxwell's equations are part of a larger set of MHD equations. We aim to approximate the MHD equation of motion

$$\rho \frac{Dv}{Dt} = -\nabla p + \rho\mathbf{g} + \mathbf{j} \times \mathbf{B}, \tag{3}$$

with bulk velocity $\mathbf{v}$, pressure p, density ρ, acceleration due to gravity $\mathbf{g}$, and magnetic field strength $\mathbf{B}$. All magnetic fields must satisfy Gauss's law for magnetism(1), which asserts that magnetic monopoles do not exist. In ideal MHD approximation, there are a number of implicit approximations taken into account. Typical plasma velocities are much less than the speed of light, c, so the first term on the right in equation (2) may be neglected

$$\nabla \times \mathbf{B} = \mathbf{4}\pi\mathbf{j}, \tag{4}$$

where $\mathbf{j}$ represents the current density (4π and c are all constants, and can be ignored for our purpose). Equation (3) calculates the motion of the plasma as a fluid. There are several approximations we can make when considering this equation in the solar corona. In static equilibrium, the time dependence vanishes, so we have $0 = -\nabla p + \rho\mathbf{g} + \mathbf{j} \times \mathbf{B}$. In the corona, the plasma pressure is much less than magnetic pressure, so we can neglect the pressure term. Finally, we can neglect gravity since length scales we are considering are much less than the pressure scale height for the corona. Thus our equation of motion is reduced to the force-free condition

$$\mathbf{j} \times \mathbf{B} = \mathbf{0}. \tag{5}$$

This is satisfied when the electric current flows parallel or anti-parallel to the magnetic field lines, that is, $\nabla \times \mathbf{B} = \mathbf{j} = \alpha \mathbf{B}$. There are three possibilities for α: $\alpha = 0$, $\alpha = constant$, and $\alpha = \alpha(\mathrm{r})$. If $\alpha = 0$, then (5) gives $\nabla \times \mathbf{B} = 0$, and consequently the current is zero. In this case, one may write $\mathbf{B} = -\nabla\phi$, where ϕ is some scalar magnetic potential. Substituting into Gauss's law gives us Laplace's equation $\nabla^2\phi = 0$. This is, by definition, a potential field, where the force field can be expressed as a gradient of a potential scalar, or $\mathbf{F}(\mathbf{r}) = \nabla\phi(\mathbf{r})$. It follows that the current vanishes in all magnetic potential fields, and that all potential fields satisfy Laplace's equation. If $\alpha = constant$, we have a linear force-free field. However, force-free fields have limitations (Su 2007). Finally, if α is a function of position, we have a nonlinear force-free field, which is what we are searching for. A NLFFF contains free magnetic energy equal to the difference between the energy in a non-potential field and the energy in a potential field. We will continue our discussion on the numerical method we use to solve these equations in section 4.

1.4. Motivation for Studying Solar Eruptions and our Project

Solar activity can be researched for a variety of reasons, the most common being the effects it can have on Earth. In particular, solar eruptions play a critical role in space weather. Richard Fisher, director of the Heliophysics division at NASA, said, "To mitigate possible public safety issues, it is vital that we better understand extreme space weather events caused by the sun's activity." The energy emitted by a solar flare completely covers the electromagnetic spectrum, ranging from high-energy gamma-rays to short radio waves. In addition to hazardous materials in space, the radiation emitted by solar flares can disrupt power lines, and can even create widespread blackouts in power grids and long-range radio communication. The heavy particles and radiation especially endanger spacecraft and astronauts whose location is beyond the Earth's protective upper atmosphere.

Scientists continue to look for ways to predict solar storm activity. An essential step required to do this is to obtain a thorough understanding of the strength and configuration of the coronal magnetic field (i.e., location where reconnection occurs). However, magnetic fields in the solar corona are generally too weak for accurate measurements, so we resort to a numerical technique. In this project, we focus on observing and modeling the magnetic field prior to and during the flare/CME event that occurred in Active Region (AR) 11060 on 2010 April 8. We compare the geometry of the coronal structures with magnetic models that are created based on the line-of-sight (LOS) magnetograms. This is achieved by matching model field lines with observed coronal loops. These loops are observed as plasma flowing along the Sun's magnetic field lines.

I began my work by becoming familiar with observations of solar eruptions, as well as the numerical modeling technique (Coronal Modeling System) developed by van Ballegooijen (2004). Our goal was to create two magnetic field models of the active region: (1) best-fit nonlinear force-free field (NLFFF) model of the region prior to the eruption; and (2) unstable state of the magnetic fields present at the onset of the event. The best-fit NLFFF model will be constrained by the observed corona loops. The unstable state model will be compared with the locations of flare footpoints and ribbons at the event onset, and we will attempt to correlate these features with certain field lines in the model. This paper is organized as follows. Section 2 describes briefly the instruments we are using. We present the observations of the flare in Section 3. The modeling procedures and results are shown in Section 4, and a short summary is given in Section 5.

2. Data Set and Instruments

In this project we use observations at various wavelengths. The instruments include the Atmospheric Imaging Assembly (AIA) and Helioseismic and Magnetic Imager (HMI) aboard the *Solar Dynamics Observatory* (SDO), and the X-Ray Telescope (XRT) aboard *Hinode*.

2.1. *Solar Dynamics Observatory*

The SDO was launched on February 11, 2010, 10:23 am EST on an Atlas V from SLC 41 from Cape Canaveral. It is the first mission to be launched for NASA's Living With a Star (LWS) Program, a program designed to understand the causes of solar variability and its impacts on Earth. SDO is designed to help us understand the Sun's influence on Earth and Near-Earth space by studying the solar atmosphere on small scales of space and time and in many wavelengths simultaneously. SDO's goal is to understand, driving towards a predictive capability, the solar variations that influence life on Earth and humanity's technological systems by determining how the Sun's magnetic field is generated and structured, and how this stored magnetic energy is converted and released into the heliosphere and geospace in the form of solar wind, energetic particles, and variations in the solar irradiance.

2.1.1. Atmospheric Imaging Assembly

The AIA aboard SDO consists of seven Extreme Ultraviolet (EUV) and three Ultraviolet (UV)-visible channels. The mission is designed to provide an unprecedented view of the solar

corona, taking images that span at least 1.3 solar diameters in multiple wavelengths nearly simultaneously, at a resolution of about $0.''6$ pixel^{-1} and at a cadence of 12 seconds or better. The primary goal of the AIA Science Investigation is to use these data, together with data from other instruments and from other observatories, to significantly improve our understanding of the physics behind the activity displayed by the Sun's atmosphere, which drives space weather in the heliosphere and in planetary environments. The AIA will produce data required for quantitative studies of the evolving coronal magnetic field, and the plasma that it holds, both in quiescent phases and during flares and eruptions; the AIA science investigation aims to utilize these data in a comprehensive research program to provide new understanding of the observed processes and, ultimately, to guide development of advanced forecasting tools needed by the user community of the Living With a Star (LWS) program.

2.1.2. Helioseismic and Magnetic Imager

HMI is an instrument designed to study oscillations and the magnetic field at the solar surface, or photosphere. HMI is one of three instruments on SDO; together, the suite of instruments observes the Sun nearly continuously and takes 1.5 terabytes of data a day. HMI observes the full solar disk at 6173 Å with a resolution of $0.''5$ pixel^{-1}. HMI is a successor to the Michelson Doppler Imager on the *Solar and Heliospheric Observatory*.

Further information on the *Solar Dynamics Observatory* and its missions can be found on the SDO website[1], where most of the information on these instruments was obtained.

2.2. *Hinode*/XRT

Hinode is a Japanese mission developed and launched by *ISAS/JAXA*, with *NAOJ* as domestic partner and *NASA* and *STFC* (UK) as international partners. It is operated by these agencies in co-operation with *ESA* and the *NSC* (Norway)."

The X-Ray Telescope (XRT) onboard *Hinode* is a high-resolution grazing-incidence telescope, which is a successor to the highly successful *Yohkoh* Soft X-Ray Telescope (SXT). A primary purpose of the *Hinode*/XRT is to observe the generation, transport, and emergence of solar magnetic fields, as well as the ultimate dissipation of magnetic energy in forms such as flares and pico-flares, coronal heating, and coronal mass ejections. XRT observes the dissipation part of the life-cycle story of solar magnetic fields. High-resolution soft X-ray

[1] *http://sdo.gsfc.nasa.gov/*

images reveal magnetic field configuration and its evolution, allowing us to observe the energy buildup, storage and release process in the corona for any transient event. One of the unique features of XRT is its wide temperature coverage to see all the coronal features that are not seen with any normal incidence telescope. These temperatures range anywhere from 1 MK to 10 MK. XRT also consists of visible light optics for alignment purpose.

For more information on the *Hinode*/XRT, please visit the XRT website[2], which provides the description used here.

3. Observations of the Flare

In this section we introduce observations of the flare/CME event provided by SDO/AIA. Figure 4 shows images from three AIA channels at different stages of the eruption. The top 4 images are from 193 Å, the middle are from 94 Å, and the bottom are of 304 Å. These channels were specifically selected for the different views of the sun that they capture. AIA 193 Å is generally well-suited for observing pre-flare loops, AIA 304 Å displays the flare ribbons especially well, and AIA 94 Å clearly depicts post-flare loops at the early phase of the flare. In the first column, a pre-flare image is displayed. In each image, the photo was taken ∼5 minutes before the flare onset. This was about the time in each channel where the flare first showed signs of activity. The second column displays observations from 02:40 UT, 10 minutes after the flare onset. In this stage, the flare ribbons are visible in 193 Å and 304 Å, and remain close to each other, while the flare loops are visible in 94 Å. As the flare continues to erupt, the new magnetic field lines reconnect at higher and higher altitudes (Svestka and Cliver 1992), and the ribbons become further separated from one another (third column of Figure 4). At about 03:15 UT (not shown in figure), the first signs of dimmings appear in AIA 193 Å, about 15 minutes after the observations in the third column. After the eruption is well underway, post-flare loops are visible in all channels (last column). The last images were all taken over three hours after the flare onset.

[2] *http://xrt.cfa.harvard.edu/*

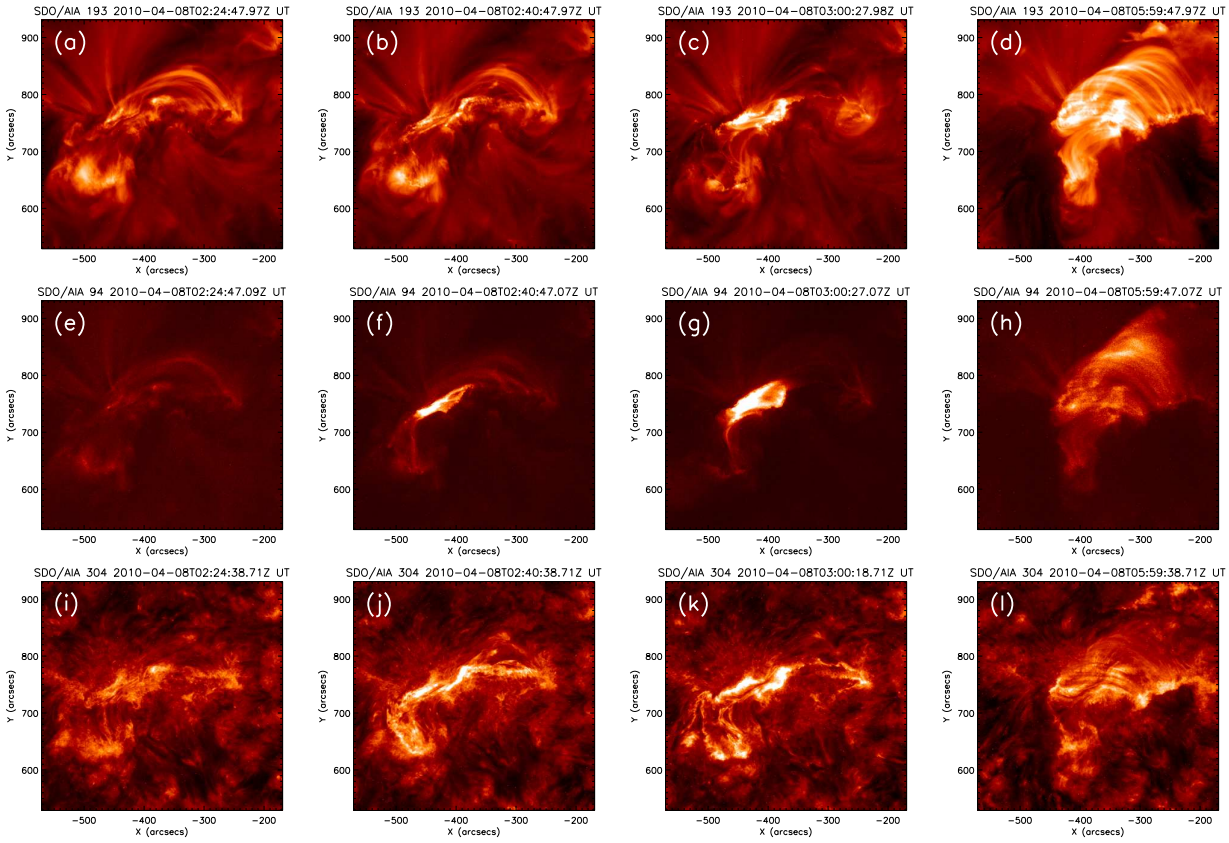

Fig. 4.— SDO/AIA Observations of the flare/CME event on 2010/04/08 at three different wavelengths. (a)-(d) show the event at 193 Å. The second row depicts the flare at 304 Å, while the last row is of AIA 94 Å. Each row contains a pre-flare image, an image where the ribbons are close to one another, one when they are further apart, and finally an image depicting the post-flare loops.

4. Magnetic Field Modeling

4.1. Flux Rope Insertion Method

At the end of Section 1.3, we explained our goal of creating a NLFFF. The magnetic field in the photosphere is not force free, and the highly sheared field in the filament channel is not always visible in the photosphere where the vector field measurements are made (Su et al. 2009b). Therefore, we resort to a numerical modeling technique which solves $\nabla^2\phi = 0$. In the present study we use Coronal Modeling System, a software that constructs models of the coronal magnetic field and compares them with observations. Using this program, we construct NLFFF models using the flux rope insertion method (van Ballegooijen 2004). The flux-rope insertion method only requires LOS photospheric magnetograms, i.e. only

the radial component of the magnetic field in the photosphere (Savcheva & van Ballegooijen 2009).

This method involves inserting a magnetic flux rope into a potential-field model. First a modified potential field is constructed, based on observations of the photospheric magnetic field. The potential field represents the coronal arcade that overlies the flux rope and prevents it from erupting into the heliosphere (Bobra et al. 2008). The next step is to specify the parameters of the flux rope, including its path on the solar surface and its axial and poloidal fluxes. The path selection is guided by the observed location of the filament in the Hα images. The path starts in the positive polarity on one side of the PIL, follows the PIL along the observed filament, and ends on the negative polarity on the other side of the PIL. We then modify the potential field so as to create a cavity in the region above the selected path. In essence, the field lines immediately above the path are pushed upward, creating a region with $\mathbf{B} \approx 0$. The flux rope is then inserted into this cavity. The axial flux is represented by a thin tube that runs horizontally along the length of the selected path (at a small height above the photosphere). At the two ends of the path, the tube is anchored in the photosphere via two vertical sections. The poloidal flux is inserted as a set of closed field lines that wrap around this tube.

The above field configuration is not in force-free equilibrium, so the next step is to relax it to an equilibrium state using a process called magneto-frictional relaxation (van Ballegooijen 2004). Magnetofriction has the effect of expanding the flux rope until its magnetic pressure balances the magnetic tension applied by the surrounding potential arcade (Savcheva & van Ballegooijen 2009). This is done by adding an artificial friction term to relax the system to equilibrium. The equation of motion during this relaxation takes the modified form

$$\rho \frac{D\boldsymbol{v}}{Dt} = -\nabla p + \rho \mathbf{g} + \mathbf{j} \times \mathbf{B} - \mu \boldsymbol{v} \tag{6}$$

After canceling out the appropriate terms, we are left with $\mu \boldsymbol{v} = \mathbf{j} \times \mathbf{B}$. The added frictional term shows that $\boldsymbol{v} \propto \mathbf{j} \times \mathbf{B}$. When the plasma eventually stops moving, $\mathbf{j} \times \mathbf{B} = \mathbf{0}$, and the flux rope will be in equilibrium. One Fortran program is used to perform magneto-frictional relaxation, and to produce the NLFFFs. However, not all models converge to a force-free state. A loss of equilibrium can occur when the poloidal and axial fluxes exceed a certain value (threshold); When this happens, the field expands indefinitely and erupts as a CME (Su et al. 2009a).

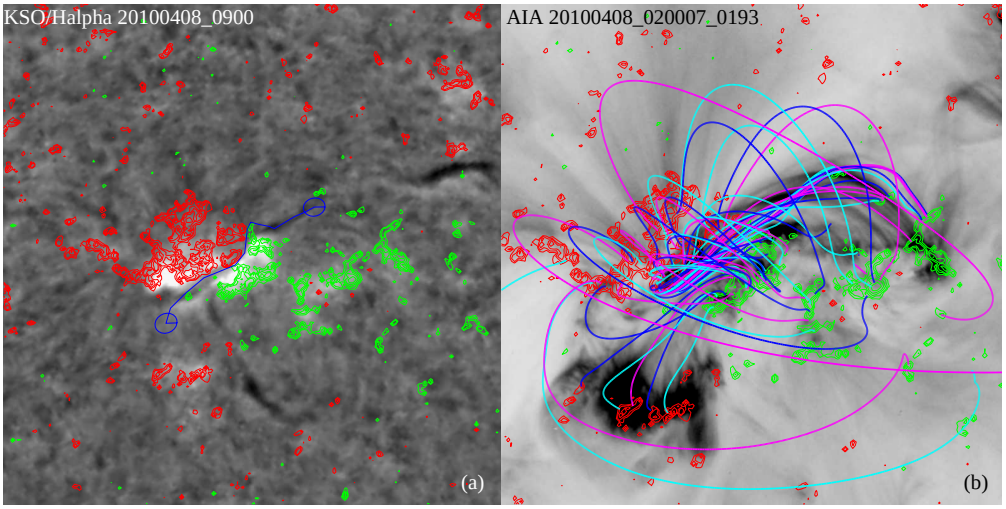

Fig. 5.— (a) Flux rope path selected over Hα image provided by Kanzelhhe Solar Observatory, separating the two regions of opposite magnetic polarity. In (b), sample field lines from one model are overlaid on an AIA 193 Å image.

4.2. Finding the Threshold

Our first task was to find the threshold. We began this process by creating three NLFFF models. Each model has a poloidal flux of 1×10^{10} Mx cm^{-1}, and all have identical flux rope paths. Figure 5(a) shows the path selected over an Hα image. The contours represent the magnetic field strength, which remains constant along each contour, and decreases along each larger contour. The path was selected along the Hα filament, which can be seen as a darker line dividing the regions of opposite magnetic polarity. Figure 5b shows an example of a model flux rope along the PIL, along with the overlying field lines holding it down. This figure also depicts sample field lines starting from the positive (red) polarities and ending at the negative (green) ones. The three models have axial fluxes of 3×10^{20} Mx, 6×10^{20} Mx, and 9×10^{20} Mx respectively. Our goal in this stage was to find the threshold, the value of the axial flux where the flare/CME first showed signs of erupting. This was accomplished by looking at 2D gray images of the current and comparing height and structural differences throughout the relaxation (iteration) process. To obtain a 2D plot, we took a vertical slice of the plane, orthogonal to the direction of the flux rope. If the height of the flux rope was still increasing after 30,000 iterations, or if there were signs that reconnection had occurred, that would imply that the flux rope would eventually lift off and form a CME. If throughout the 30,000 iterations the flux rope's height had reached a maximum, or if there were no significant structural differences in the configurations, that would show that our model had reached an equilibrium state.

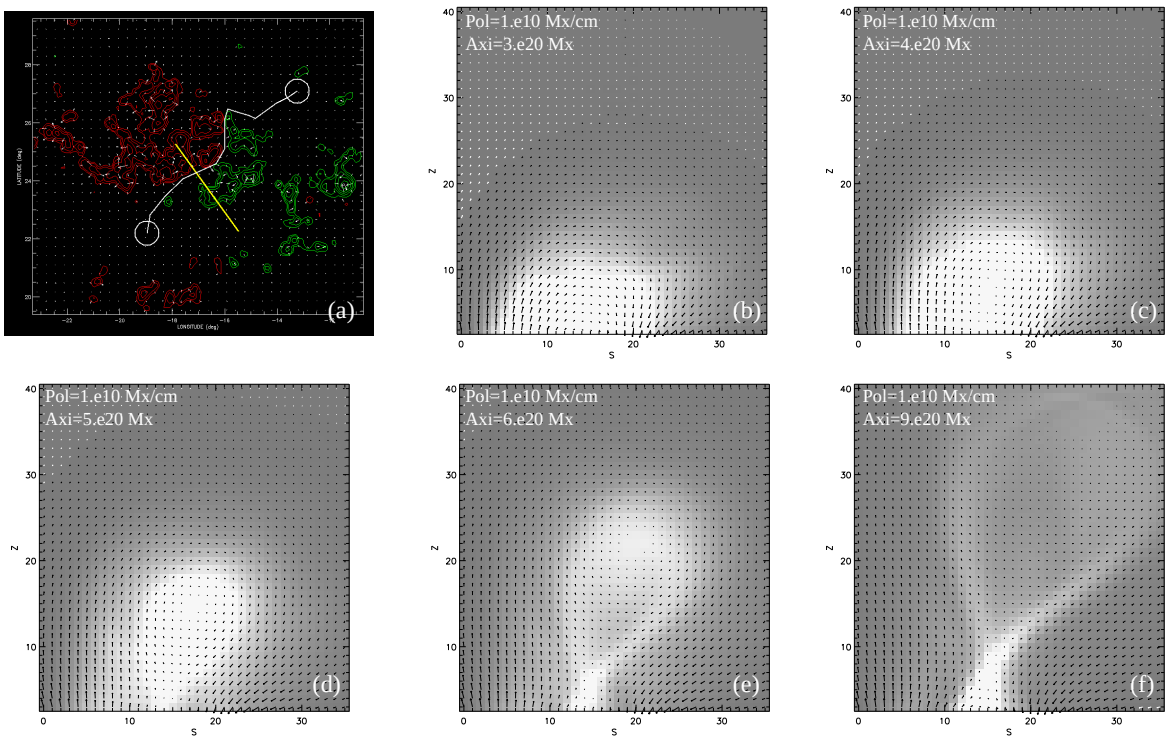

Fig. 6.— Panel (a) shows the slice used to observe the models in the 2D plane. Panels (b) through (e) show 2D images of five different models. Every model is shown after 30,000 iterations.

Figure 6 shows the location of the slice that we used to obtain the 2D images, along with all the models we created. Model 1 (Φ_{axi} = 3×10^{20} Mx) appeared to be very stable, with little structural difference throughout the relaxation process, while the flux rope in model 3 (Φ_{axi} = 9×10^{20} Mx) clearly was erupting. The similarities between the structures from Figure 6f and Figure 3 further proves that this model is unstable. Model 2 (Φ_{axi} = 6×10^{20} Mx) was also unstable and in the process of erupting, as shown by the sign of reconnection occurring near the bottom of the image (Figure 6e). This implied that our threshold had an axial flux somewhere between 3×10^{20} Mx and 6×10^{20} Mx. Based on these results, we created model 4 and model 5, with axial fluxes of 4×10^{20} Mx and 5 × 10^{20} Mx respectively. All the models shown in the figure are relaxed after 30,000 iterations. The white regions represent where the current is strong in each model. The models in Figure 6b and 6c are both stable, with no significant change in their 2D structure. The last three images all have a distinct area near the bottom, corresponding to the magnetic reconnection site, implying these models have already erupted. From this figure, we determined that model 5 (Φ_{axi} = 5×10^{20} Mx) is the marginally stable state. This is the axial flux value we use for the

threshold.

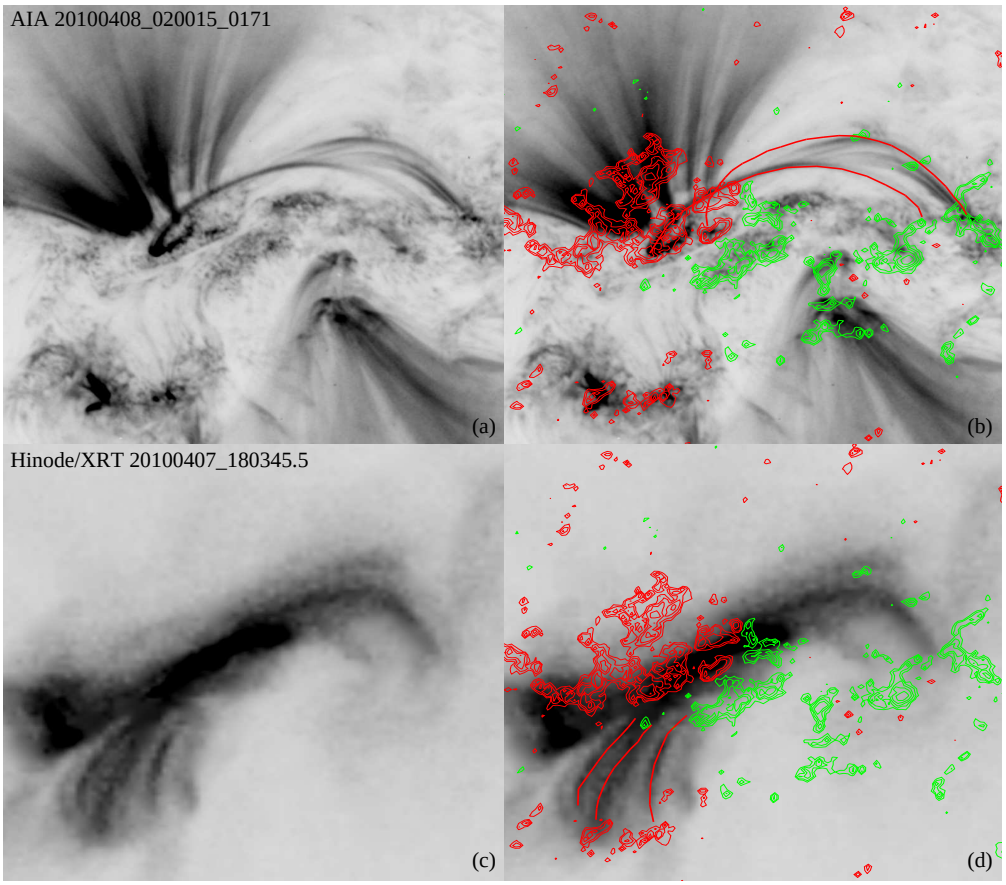

Fig. 7.— Images used for selecting coronal loops: (a) AIA 171 Å at 02:00 UT and (c) XRT observation. The red lines in the second column show Loops 1 and 2 (b) traced manually over the coronal loops in AIA 171 Å, and Loops 3, 4, and 5 (d) over the XRT image.

4.3. Pre-flare NLFFF Model

Our next step was to use our data of the event to locate non-potential coronal loops that we could compare with our models to search for a best-fit NLFFF model prior to the eruption. We expect this model to be a stable model ($\Phi_{axi} < 5{\times}10^{20}$ Mx), but we also consider models at or just above the threshold as well. We looked at AIA images at different channels from around 02:00 UT (∼30 minutes before the flare began to erupt), along with XRT photos, to locate the coronal loops we would use for our comparison. Figure 7 shows AIA 171 Å and XRT image (Figure 7a and 7c) where most of the selected loops were observed. The red lines

in the second column show the loops traced manually using CMS. We chose Loop 1 from the AIA 171 Å image, and Loop 2 from the AIA 193 Å image. These specific channels were chosen since each clearly displayed loops across the middle of the images. The last three loops (Loops 3, 4, and 5) were selected from a *Hinode*/XRT image taken at 18:03:45 UT the night before the flare. This image clearly depicted three loops near the bottom of the photograph. We assign Loop 3 to be the loop on the left, Loop 4 in the middle, and Loop 5 as the loop on the right.

Table 1: The Average Deviations (AD) of the model field lines from the observed EUV Loops (1, 2) and X-ray Loops (3, 4, and 5) for various models of AR 11060 on 2010 April 8. The * symbol indicates a misleading AD value.

		Φ_{axi} (10^{20} Mx)			
		3	4	5	6
Loop	F_{pol} (10^{10} Mx cm^{-1})	AD$\pm$ 0.2 (10^{-3} R_{sun})			
Loop 1	1	3.2	2.4	2.2	2.6*
Loop 2	1	2.9	2.7	4.1	8.2
Loop 3	1	3.5	0.7	0.4*	0.5*
Loop 4	1	1.4	0.3	1.1	2.9
Loop 5	1	3.3	1.1	0.4	0.6

Each coronal loop was then compared with model 1, model 2, model 4, and model 5. We did not compare with model 3 ($\Phi_{axi} = 9\times10^{20}$) since its axial flux was much higher than the threshold, and thus would not fit the criteria for what we were looking for. We tested different field lines by clicking on various points along the observed loops from Figures 7(b) and (d) and then noting the average deviation (AD) between the two (CMS automatically produces field lines that travel through the location of our selection). The AD is in units of solar radii. We selected hundreds of different field lines, aiming to get both small AD values and field lines that matched structurally with the coronal loops. Table 1 shows the AD between the field lines from the models we created and the observed coronal loops.

Although some models had small ADs, they did not fit the observed loops structurally. Any comparisons marked with a * imply that the field lines were either much longer than the coronal loops, or they traveled in the wrong direction; In either case, the models marked with that symbol should not be taken into consideration for the best-fit pre-flare model. We use this approach when comparing models 4 and 5 (axial flux values of 4×10^{20} Mx and 5×10^{20} Mx, respectively), since both appear to be accurate models when viewing only the AD. However, there are no field lines in model 5 that accurately match Loop 3. Alternatively,

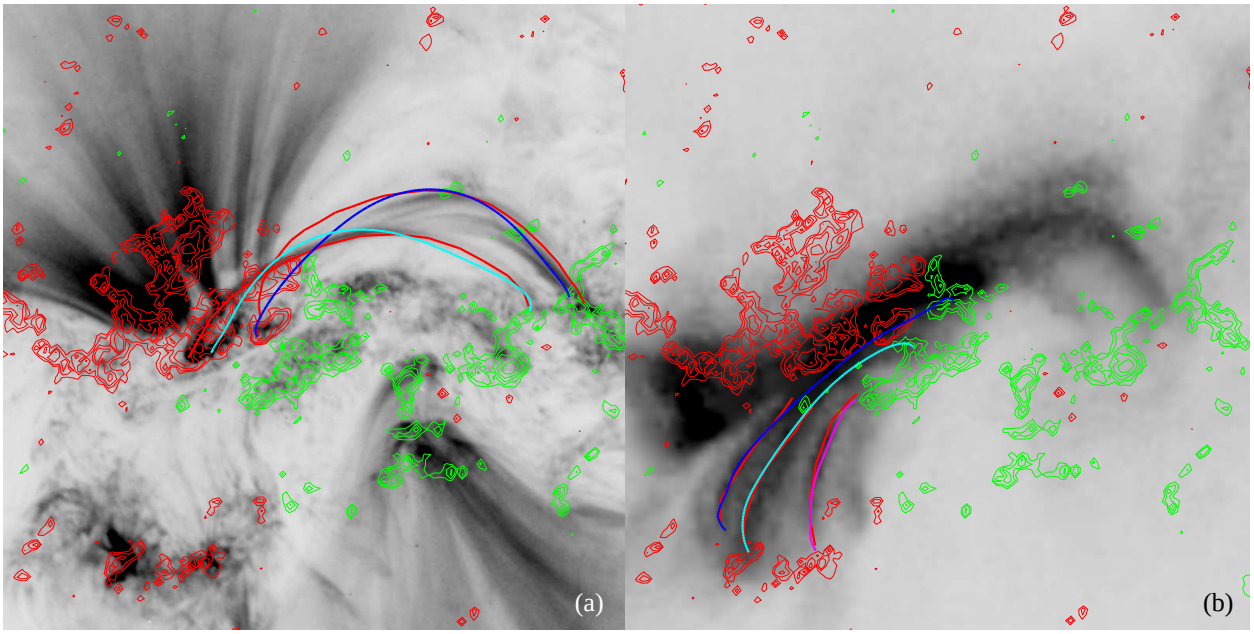

Fig. 8.— Best-fit model field lines from model 4 shown over the manually traced coronal loops (red lines) from Figure 6b and 6d.

model 4 (fourth column in Table 1) has very low ADs, and fits each of the coronal loops very well. Therefore, this is the model we designate as our pre-flare model, confirming our expectation that the best-fit model prior to the eruption was stable.

Figure 8 shows the selected coronal loops along with the best-fit field lines from model 4. Figure 8a is of AIA 171 Å at 02:00 UT while Figure 8b consists of the XRT image that we selected the last three loops from. The similarities from the observed coronal loops and the theoretical field lines demonstrates that we have an excellent model. Although the field lines in (d) extend further than the observed loops were drawn, this does not contradict our work. We expect the coronal loops to be longer, but are unable to draw them accurately after a certain region of the image due to the saturation.

4.4. Model at the Early Stage of the Flare

The second model we were searching for was an unstable model during the early stages of the event onset. This model would be selected based on its axial flux; we want it to have an axial flux just past the threshold. For our study, this corresponds to model 2 ($\Phi_{axi} = 6 \times 10^{20}$ Mx). Figure 9 shows this model throughout the relaxation process. We ran this model for an

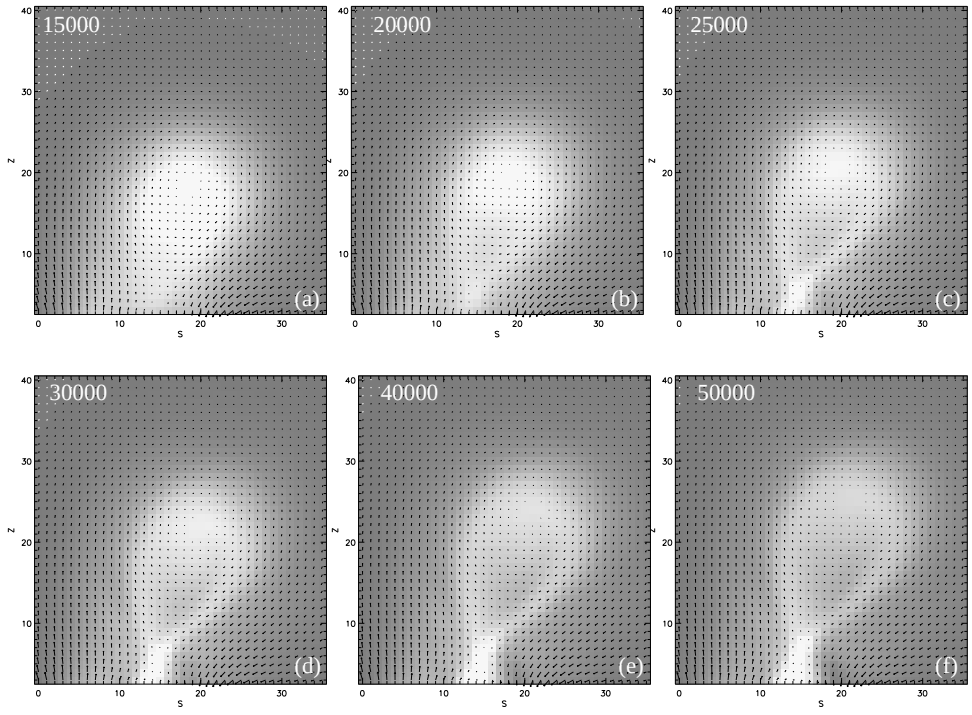

Fig. 9.— A vertical slice of the current plot for model 2 with poloidal flux of 1×10^{10} Mx cm^{-1} and axial flux of 6×10^{20} Mx displayed at six different stages during the relaxation process. The number of iterations is shown in the top left in each panel.

additional 20,000 iterations to observe the expansion of the flux rope in greater detail. The reconnection site is also growing in each successive image, supporting the theory of magnetic reconnection. The electric current appears to be more spread out towards the boundary of the flux rope, possibly due to the flux rope being larger, and thus less dense.

In Figure 10 we attempt to correlate features from the event with certain field lines from our unstable model. We show images from AIA 94 Å (top row) and AIA 193 Å (bottom row). This figure shows a graphical example of the two different segments of the flux rope after it has erupted. The bottom part below the reconnection site is where the post-flare loops form, while the top part is the expanding CME. Figure 10a shows post-flare loops at 02:39 (UT), about 9 minutes after the eruption began. In Figure 10b, newly reconnected field lines from below the reconnection site are shown. These field lines are direct results from the different points that were clicked in the 2D image in Figure 10c. The field lines in Figure 10(b) closely match the observed loops in Figure 10a. In the second row, Figure 10d shows two dark regions on the left and right of the main event, corresponding to regions of coronal dimming. These regions are thought to be the footpoints of the expanding flux

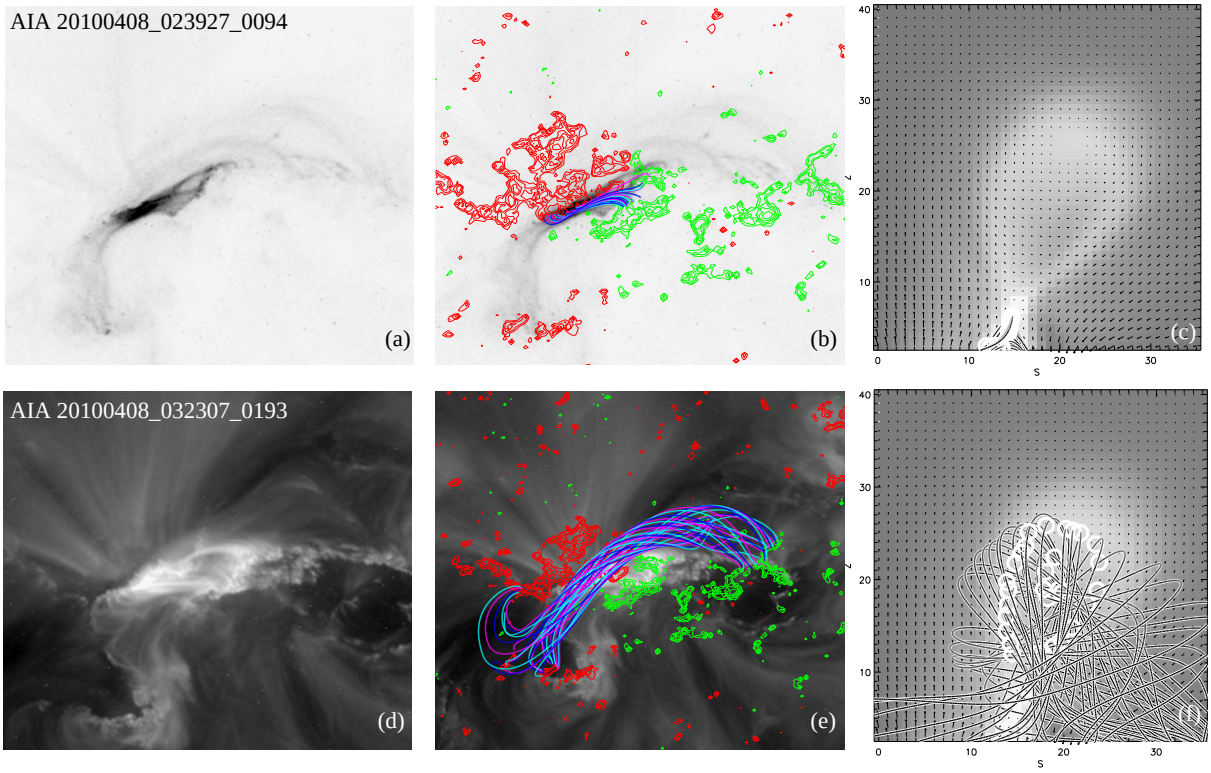

Fig. 10.— AIA Å image at 02:39 (UT) is displayed in (a). (b) shows the same image overlaid with the "bottom" segment of the flux rope that is left behind after reconnection. Field lines in this image are produced from the selections made underneath reconnection point in (c). AIA 193 Å image at 03:23 (UT) showed in second row. Coronal dimming regions are visible in (d) and (e) as footpoints of the expanding flux rope. Panel (f) shows the location of our selected clicks to produce the flux rope in (e).

rope, which we clearly see to be the case in Figure 10(e). This supports the current theory of the relationship between CMEs and dimmings. This flux rope was produced by clicking on different areas above the reconnection site in Figure 10(f). The post-flare loops and newly reconnected field lines in the top row, along with the coronal dimmings and expanding flux rope in the bottom row, all demonstrate the accuracy of our unstable model.

5. Summary

Using the flux rope insertion method, we constructed a series of NLFFF models for AR 11060 of a flare/CME event on 2010 April 8. Only LOS photospheric magnetograms were required to create the models. We used data from Hinode/XRT, SDO/AIA, SDO/HMI, and

Hα observations. We created five models, searching for (1) best-fit nonlinear force-free field model (NLFFF) of the region before the eruption; and (2) unstable state of the magnetic fields present at the onset of the event. We found the threshold to have an axial flux of 5×10^{20} Mx (model 5). We then searched for our best-fit NLFFF model, expecting it to be stable. This proved to be the case, as our best-fit model had an axial flux of 4×10^{20} Mx, a slightly smaller value than the threshold. Model 4 contains a highly sheared and weakly twisted flux rope, which is in equilibrium with the overlying magnetic field. The close proximity of the axial flux value from model 4 and the axial flux from the threshold indicates that our model is very close to losing equilibrium. The unstable model ($\Phi_{axi} = 6 \times 10^{20}$ Mx) matches the observations at the early phase of the flare very well. The coronal dimming regions were located at the footpoints of the expanding flux rope, further showing the accuracy of our model. All of these results strongly support that the event that occurred on 2010 April 8 in AR 11060 was due to the loss-of-equilibrium mechanism.

6. Acknowledgments

It is a pleasure to thank those who made this paper possible. I would first like to thank my advisor, Dr. Yingna Su, for her help and support during this REU. I am also very grateful to Dr. Aad van Ballegooijen for his guidance and knowledge he offered me throughout this program. Finally, I would like to thank the NSF and the Harvard-Smithsonian Center for Astrophysics for the valuable research experience I obtained through this internship.

REFERENCES

Antrill, G., 2008, 'Low Coronal Signatures of Coronal Mass Ejections', PhD thesis (p. 55), University College London

Aschwanden, M. J. 2005, Physics of the Solar Corona

Bobra, M. G., van Ballegooijen, A. A., & DeLuca, E. E. 2008, ApJ, 672, 1209

Cliver, E. W., Dennis, B. R., Kiplinger, A. L., Kane, S. R., Neidig, D. F., Sheeley, N. R., Jr., & Koomen, M. J. 1986, ApJ, 305, 920

Eddy, J. A. 2009, The Sun, the Earth and Near-Earth Space: A Guide to the Sun-Earth System. ISBN 978-0-16-08308-8. pp. 301,

Forbes, T. G. 2000, J. Geophys. Res., 105, 23153

Hansen, R. T., Garcia, C. J., Hansen, S. F., & Yasukawa, E. 1974, PASP, 86, 500

Harvey, K. L. 1996, American Institute of Physics Conference Series, 382, 9

Priest, E. R. 1984, Solar Magneto-hydrodynamics, Dordrecht: Reidel, 1984,

Sandell, J., Kashyap, V., Weber, M., van Ballegooijen, A., Deluca, E., & Bobra, M. 2006, Bulletin of the American Astronomical Society, 38, 918

Savcheva, A., & van Ballegooijen, A. 2009, ApJ, 703, 1766

Sterling, A. C., & Hudson, H. S. 1997, ApJ, 491, L55

Su, Y., van Ballegooijen, A., Lites, B. W., Deluca, E. E., Golub, L., Grigis, P. C., Huang, G., & Ji, H. 2009, ApJ, 691, 105

Su, Y., van Ballegooijen, A., Schmieder, B., Berlicki, A., Guo, Y., Golub, L., & Huang, G. 2009, ApJ, 704, 341

Su, Y., 2007, 'Magnetic Shear in Two-ribbon Solar Flares', PhD thesis, Purple Mountain Observatory.

Svestka, Z., & Cliver, E. W. 1992, IAU Colloq. 133: Eruptive Solar Flares, 399, 1

Tang, F. 1985, Sol. Phys., 102, 131

van Ballegooijen, A. A. 2004, ApJ, 612, 519

Zhukov, A. N., & Auchère, F. 2004, A&A, 427, 705